JOURNAL OF COMPUTATIONAL PHYSICS 113, 291–303 (1994)

The Numerical Computation of Singular Minimizers in Two-Dimensional Elasticity

PABLO V. NEGRÓN-MARRERO

University of Puerto Rico, Department of Mathematics, Rio Piedras, Puerto Rico 00931

AND

OCTAVIO BETANCOURT

Department of Computer Science, City College, CUNY, New York, New York 10031

Received January 19, 1993; revised October 1, 1993

In this paper we use a spectral-collocation method for the computation of singular minimizers in two-dimensional elasticity. In particular we are interested in computing cavitating solutions (those that open a hole at the center) and determining whether or not they are globally stable in the energy sense. We describe the spectral collocation method which is used in conjunction with a Richardson extrapolation iteration and discuss various aspects related to the convergence of the method. We obtain a variety of results for certain ranges of parameters that show how the size of the cavitation depends on these parameters.

1. INTRODUCTION

The phenomena of void formation on bodies in tension have been observed among others by Gent and Lindley [8]. Ball [1] showed in the context of nonlinear elasticity, that void formation or "cavitation" can decreased the (potential) energy of a body in tension when the tension is sufficiently large. In fact for a spherical body composed of isotropic material, when the tension is sufficiently large, the purely radial deformation that opens a hole at the center of the ball, is a global minimizer among such deformations. It remains as an open question if such radial solutions are actually global minimizers over an appropriate space of deformations without radial symmetry. James and Spector [12] proved for a certain class os stored energy functions that includes the ones in the works of Sivaloganathan [13] and Stuart [14], that the radial minimizer is not a global minimum among functions without radial symmetry. In fact they showed that by opening a small "cylindrical" hole in the material (outside the cavity), the energy of the resulting deformation is smaller than the radial deformation.

The numerical aspects of cavitation and other singular minimizers in elasticity are very delicate. It has been observed that, because of the so-called Lavrentiev phenomena [9], the usual finite element methods can fail to compute both the minimizer and the minimum energy. A numerical method for overcoming the Lavrentiev phenomenon has been proposed by Ball and Knowles [2] and Negrón-Marrero [10]. This method uses a decoupling on the deformation gradient that works quite well for one-dimensional problems, but that for higher dimensional problems, after discretization, yields a large scale constrained optimization problem. To handle numerically this problem effectively one would need to use, for instance, multigrid methods and exploit the sparsity of the resulting discrete equations.

Instead of taking this approach, we proceed in this work by discretizing the energy functional using finite differences in the one-dimensional case and a spectral method (finite differences in the radial direction and a truncated Fourier series for the angular variable) for the two-dimensional problem. We then minimize the resulting discrete functionals with an iterative scheme based on a second-order Richardson extrapolation. We show for the example of Ball and Knowles [2] that the discrete energy functional has two local minimizers, one that is global and is an approximation of the singular minimizer of the continuous problem and the other is an approximation of the smooth solution of the Euler–Lagrange equation found numericaly by Ball and Knowles. Both of these solutions are computed by the numerical scheme, depending on the initial condition even for relatively small meshes. Thus for the discrete problem the Lavrentiev phenomena reduces to the case of a functional with two local minima, one being global and the other local. We estimated the domain of attraction of each minima by using functions of the form $x^{1/2}$ as initial guess in

0021-9991/94 $6.00

the iterative scheme. We found that for this class of functions the domain of attraction is essentially independent of the mesh size (see Fig. 3.2.).

The elasticity problem treated in Sections 5 and 6 is a free boundary value problem, where the free boundary condition is given by the natural boundary conditions at the center of the plate (cf. (5.8) and (6.7)). The corresponding discretizations of these free boundary conditions can be obtained by minimizing the discrete functional with respect to the cavity size (for radial solutions) or with respect to the cavity shape (in the full two-dimensional case). The solutions in our problem are singular in the sense that they are discontinuous at the origin ($R(0, \theta) \neq 0$, cf. (4.10)) when a cavity (not necessarily circular) appears. Thus no special treatment is required in its representation (in polar coordinates) in the numerical calculation, besides the use of the free boundary condition.

The structure of the paper will be as follows. In Section 2 we discuss a numerical method for finding local minima of our discrete problems. The method we use is an iterative scheme based on a second-order Richardson extrapolation technique (see Garabedian [7]). In Section 3 we will revisit the example in Ball and Knowles, obtain a discrete functional, and describe in some more detail the two minima phenomena mentioned above. In Section 4 we describe a two-dimensional model for nonlinear elasticity and define a class of stored energy functions which allows for cavitation according to the results in Ball [1]. In Section 5 we discuss a finite difference discretization of the energy functional of Section 4 when the deformation is restricted to be radially symmetric. We obtain a variety of results for certain ranges of parameters that show how the size of the cavitation depends on these parameters. In Section 6 we discuss the discretization of the two-dimensional energy functional for arbitrary deformations. We describe the spectral collocation method which is used in conjunction with the Richardson extrapolation iteration. We discuss various aspects related to the convergence of the method both in the "artificial time" and with the mesh size.

Notation. $W^{1,r}(a, b)$ denotes the Sobolev space of functions in $L^r(a, b)$ which have generalized or weak derivatives that also belong to $L^r(a, b)$. For any function $f(x_1, ..., x_n)$ of n variables we write

$$f_{,i}(x_1, ..., x_n) = \frac{\partial f}{\partial x_i}(x_1, ..., x_n),$$

for the ith partial derivation, $1 \leqslant i \leqslant n$.

2. AN ACCELERATED STEEPEST DESCENT METHOD

In this section we describe an accelerated steepest descent method based on a second-order Richardson extrapolation formula. Although the description of the method can be done for any functional, we choose for simplicity to do the presentation for the Dirichlet functional. Thus we consider the problem of minimizing the functional

$$I(u) = \tfrac{1}{2} \int_\Omega (u_x^2 + u_y^2)\, dx\, dy, \tag{2.1}$$

where u belongs to some space of smooth functions and is subjected to Dirichlet boundary conditions. The first variation of I at u acting on v can be written as

$$\delta I(u) \cdot v = -\int_\Omega (\Delta u)\, v\, dx\, dy. \tag{2.2}$$

It is well known that at a minimum of (2.1) we must have

$$\Delta u = 0 \qquad \text{in } \Omega, \tag{2.3}$$

subject to some boundary conditions. The steepest descent method for minimizing (2.1) would then take the form

$$u^{k+1} = u^k + \lambda\, \Delta u^k, \qquad k = 0, 1, 2, ..., \quad u^0 \text{ given}, \tag{2.4}$$

where $\lambda > 0$. Note that

$$\delta I(u^k) \cdot (\lambda\, \Delta u^k) = -\lambda \int_\Omega (\Delta u^k)^2\, dx\, dy < 0; \tag{2.5}$$

thus $\lambda\, \Delta u^k$ is indeed a descent direction.

Let L_h, for a given mesh size h, denote a discretization of Δ (by finite differences, say). Let u_h denote a mesh function and in (2.4) write $\Delta t = \lambda$. Then (2.4) becomes

$$\frac{u_h^{k+1} - u_h^k}{\Delta t} = L_h(u_h^k), \qquad k = 0, 1, ..., \quad u_h^0 \text{ given}. \tag{2.6}$$

Thus the iteration step "k" can be viewed as a discretization of an artificial time variable "t" and (2.6) is the discretization of the heat equation

$$w_t = \Delta w \qquad \text{in } \Omega, \tag{2.7}$$

where the function w is a function of (x, y, t). The solution $u(x, y)$ in (2.3) is a steady state solution of (2.7), namely,

$$u(x, y) = \lim_{t \to \infty} w(x, y, t). \tag{2.8}$$

The Courant–Friedrichs–Lewy stability condition for (2.6) requires that $\Delta t = O(h^2)$, which makes the convergence in

(2.6) slow when h is small. To overcome this problem one considers instead of (2.7), the hyperbolic equation

$$w_{tt} + \varepsilon w_t = \Delta w \qquad \text{in } \Omega. \tag{2.9}$$

One can show (see [7]) that when ε is small, then the convergence in (2.8) is exponential in t. Moreover, the Courant–Friedrichs–Lewy stability condition for (2.9) requires that $\Delta t = O(h)$, which makes the convergence in t faster. We can now discretize (2.9) as

$$\frac{u_h^{k+1} - 2u_h^k + u_h^{k-1}}{(\Delta t)^2} + \varepsilon \frac{u_h^{k+1} - u_h^k}{\Delta t} = L_h(u_h^k), \qquad k = 1, 2, \ldots,$$
$$u_h^0, u_h^1 \text{ given}, \tag{2.10}$$

which is referred to as the *second-order Richardson method.* Although in our derivation of (2.10), L_h represents a discretization of Δ, we can use the iteration (2.10) for any nonlinear elliptic operator.

In (2.10) Δt is chosen to satisfy the Courant–Friedrichs–Lewy stability condition and the coefficient ε is chosen to achieve descent to a steady state. In practice, we have implemented an acceleration procedure that automatically optimizes the choice of ε as a function of t (see Bauer, Betancourt, and Garabedian [4, 5] and Betancourt [6]) by essentially estimating the lowest eigenvalue of L_h.

The convergence in a neighborhood of an equilibrium is given by $e^{-\lambda_i t}$ with the convergence rate λ_i related to the eigenvalue $-\omega_i^2$ of the linearized operator by

$$\lambda_i^2 + \varepsilon \lambda_i = -\omega_i^2, \qquad i = 0, 1, \ldots. \tag{2.11}$$

The optimal convergence is obtained if one chooses $\varepsilon = 2\omega_0$ where ω_0 is the lowest eigenvalue, which gives $\lambda = \omega_0$. In addition to the difficulty of not knowing the value of ω_0, the convergence rate λ_i for $i > 0$ will have a large imaginary part, resulting in oscillations and loss of descent. Moreover, this analysis breaks down in the initial phase of the iteration, when the approximation is far from equilibrium and the operator is dominated by nonlinear terms. For a globally convergent algorithm, a descent method is required with $\varepsilon \gg 1$. For these reasons, we initialize the iterates with $\varepsilon \sim 100$ and proceed to estimate the dominant eigenvalue from the time dependence itself, with the large frequencies converging quickly to zero in the initial phase of large ε, and the lowest frequencies present in the later stage with much smaller values of ε (order 0.5–1.0). This results in a gain in convergence rate of at least an order of magnitude compared to fixing ε to the initial value necessary in the nonlinear phase. The resulting scheme converges in $O(n)$ iterations. The next version of our code will incorporate a preconditioning algorithm developed by Betancourt [6] which results in a scheme requiring $O(1)$ iterations.

3. A ONE-DIMENSIONAL EXAMPLE

Consider the problem of minimizing

$$I(u) = \int_0^1 (u(x)^3 - x)^2 \, (u'(x))^6 \, dx, \tag{3.1}$$

where u belongs to the set A of absolutely continuous functions such that $u(0) = 0$ and $u(1) = 1$. Clearly with $u^*(x) = x^{1/3}$ we have that

$$I(u^*) = \min_A I(u) = 0. \tag{3.2}$$

One can show ([3]) that

$$I(u^*) < \min_{W^{1,r}} I(u), \tag{3.3}$$

for any $r > \frac{3}{2}$ which is referred to as the Lavrentiev phenomena. Because of (3.3) it has been observed that numerical schemes that typically work on Sobolev spaces with a large r (e.g., finite elements), fail to compute both the minimizer and the minimum. (See [2] for numerical results on (3.1) using a piecewise linear finite element method.)

For any integer $n \geqslant 1$, let

$$h = 1/n, \qquad x_i = ih, \qquad 0 \leqslant i \leqslant n, \tag{3.4}$$

and let u_i denote an approximation of $u(x_i)$. We consider the finite difference approximation of (3.1),

$$I_h(u_h) = h \sum_{i=0}^{n-1} \left\{ \frac{(u_{i+1}^3 - x_{i+1})^2 - (u_i^3 - x_i)^2}{2} \right\} \left\{ \frac{u_{i+1} - u_i}{h} \right\}^6, \tag{3.5}$$

where $u_h = (u_0, \ldots, u_n)$ and $u_0 = 0$, $u_n = 1$. It follows now that for any v_h with $v_0 = 0 = v_h$ we have that

$$\delta I_h(u_h) \cdot v_h = \frac{d}{d\varepsilon} I_h(u_h + \varepsilon v_h)\Big|_{\varepsilon = 0}$$
$$= h \sum_{i=1}^{n-1} [L_h(u_h)]_i \, v_i, \tag{3.6}$$

where

$$[L_h(u_h)]_i = 3(u_i^3 - x_i) \, u_i^2 \left[\left(\frac{u_{i+1} - u_i}{h} \right)^6 + \left(\frac{u_i - u_{i-1}}{h} \right)^6 \right]$$
$$+ \frac{3}{h} \Bigg[((u_i^3 - x_i)^2 + (u_{i-1}^3 - x_{i-1})^2)$$
$$\times \left(\frac{u_i - u_{i-1}}{h} \right)^5$$
$$- ((u_{i+1}^3 - x_{i+1})^2 + (u_i^3 - x_i)^2) \left(\frac{u_{i+1} - u_i}{h} \right)^5 \Bigg], \tag{3.7}$$

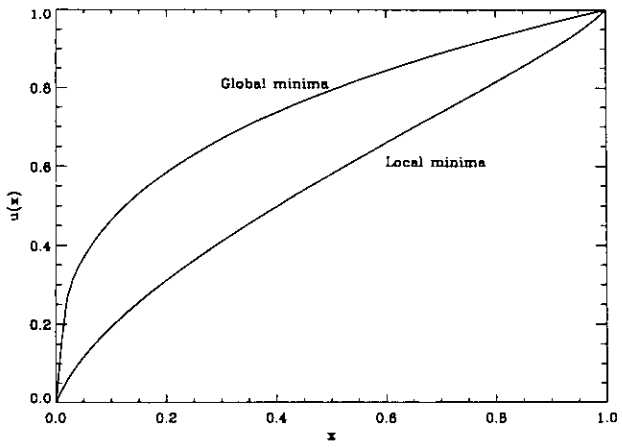

FIG. 3.1. Global (singular) and local (smooth) minima of the problem (3.1).

for $1 \leqslant i \leqslant n-1$. Note that

$$u_i = x_i^{1/3}, \qquad 0 \leqslant i \leqslant n, \tag{3.8}$$

is a global minimum of the discrete variational principle (3.5) with "discrete energy" of zero. Moreover, the accelerated steepest descent method of Section 2 (using (3.7) in (2.10)) computes both (3.8) and an approximation of a "smooth" solution of the Euler Lagrange equation of (3.1) which has a minimum value of approximately 0.0311 with $n = 40$. This second solution is a local minimum of (3.5). Both (3.8) and the computed "smooth" solution are shown in Fig. 3.1. Which solution the method computes depends on the initial point in (2.10). With $n = 40$ and

$$u_1^0 = x_1^{1/\alpha}, \qquad 0 \leqslant i \leqslant n, \quad 2.5 \leqslant \alpha, \tag{3.9}$$

one obtains (3.8). If instead of (3.9) we use

$$u_i^0 = x_i^{1/\alpha}, \qquad 0 \leqslant i \leqslant n, \quad \alpha < 2.5, \tag{3.10}$$

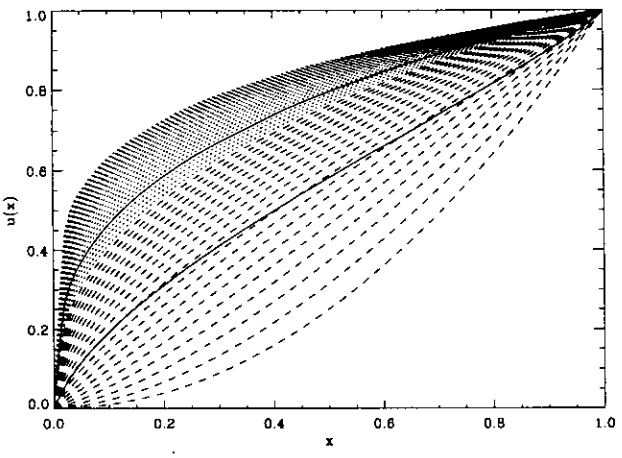

FIG. 3.2. Approximate basin of attraction for the solutions in Fig. 3.1.

then we obtain the second minima. The threshold value 2.5 was found to be essentially independent of the mesh size. The results are shown in Fig. 3.2, where (3.9) is represented by the dotted curves and (3.10) by the dashed curves.

4. A TWO-DIMENSIONAL MODEL FOR NONLINEAR ELASTICITY

We consider a body which in its reference configuration occupies the region

$$\Omega = \{x \in \mathbf{R}^2 \mid \|x\| < 1\}, \tag{4.1}$$

where $\|\cdot\|$ denotes the Euclidean norm. Let $p: \Omega \to \mathbf{R}^2$ denote a deformation of the body and let its *deformation gradient* be

$$F(x) = \frac{dp}{dx}(x). \tag{4.2}$$

The requirement that $p(\cdot)$ *preserves orientation* takes the form

$$\det F(x) > 0, \qquad x \in \Omega. \tag{4.3}$$

Let

$$M_+^{2\times 2} = \{F \in R^{2\times 2} \mid \det F > 0\}. \tag{4.4}$$

Let $W: M_+^{2\times 2} \to \mathbf{R}$ be the *stored energy function* of the material of the body. The total stored energy on the body due to the deformation p is given by

$$I(p) = \int_\Omega W(F(x))\, dx. \tag{4.5}$$

If Ω is subject to a deformation "g" on the boundary, i.e.,

$$p(x) = g(x), \qquad x \in \partial\Omega, \tag{4.6}$$

then the equilibrium configuration satisfying (4.6) minimizes (4.5) among all functions satisfying (4.3) and belonging to some appropriate Sobolev space.

A physically reasonable model for W is as follows. Let v_1, v_2 be the eigenvalues of $(F^tF)^{1/2}$ which are called the *principal stretches*. We take

$$W(F) = \Phi(v_1, v_2), \qquad F \in M_+^{2\times 2}, \tag{4.7}$$

where

$$\Phi(v_1, v_2) = Av_1^\alpha + Bv_2^\alpha + C(v_1 v_2)^\gamma + D(v_1 v_2)^{-\delta}, \tag{4.8}$$

and

$$A, B, C, D \geqslant 0, \qquad \alpha, \gamma \geqslant 1, \qquad \delta > 0. \tag{4.9}$$

If $A = B$, then the material occupying Ω is called *isotropic*.

Let (r, θ) be polar coordinates for Ω and let $(R(r, \theta), \Theta(r, \theta))$ be the polar coordinates of $p(x)$. That is, if $x = (x_1, x_2)$, then

$$p(x) = R(r, \theta)(\cos \Theta(r, \theta), \sin \Theta(r, \theta)), \tag{4.10}$$

where

$$r = \sqrt{x_1^2 + x_2^2}, \qquad \theta = \tan^{-1}(x_2/x_1). \tag{4.11}$$

The variables (r, θ) and (R, Θ) are just polar coordinates in the reference and deformed configurations, respectively. As a consequence, our equations of Sections 5 and 6 are in material or Lagrangian coordinates. An elementary computation now shows that the principal stretches v_1, v_2 are given by

$$\begin{aligned} 2v_{1,2}^2 = {} & R_r^2 + \frac{1}{r^2} R_\theta^2 + \left(\Theta_r^2 + \frac{1}{r^2}\Theta_\theta^2\right) R^2 \\ & \pm \left[\left(R_r^2 + \frac{1}{r^2} R_\theta^2 - \left(\Theta_r^2 + \frac{1}{r^2}\Theta_\theta^2\right) R^2\right)^2 \right. \\ & \left. + 4\left(R_r \Theta_r + \frac{1}{r^2} R_\theta \Theta_\theta\right)^2 R^2\right]^{1/2}. \end{aligned} \tag{4.12}$$

5. CAVITATION AMONG RADIAL DEFORMATIONS

In this section we study the case in which the deformation $p(\cdot)$ is radially symmetric, i.e.,

$$p(x) = \rho(\|x\|)\frac{x}{\|x\|}, \qquad x \in \Omega, \tag{5.1}$$

for some scalar function ρ. In this case and when $A = B$ in (4.8), then (4.12) reduces to

$$v_1 = \rho'(r), \qquad v_2 = \rho(r)/r, \tag{5.2}$$

and (4.5), (4.7) reduce (modulo 2π) to

$$I(\rho) = \int_0^1 r\Phi\left(\rho'(r), \frac{\rho(r)}{r}\right) dr. \tag{5.3}$$

From (4.3) we obtain the inequalities

$$\rho'(r), \frac{\rho(r)}{r} > 0, \qquad 0 < r < 1. \tag{5.4}$$

We assume that g in (4.6) is of the form of a uniform displacement of the boundary, i.e., for some $\lambda > 0$,

$$p(x) = \lambda e_1(x), \qquad x \in \partial\Omega, \tag{5.5}$$

where $e_1(\cdot)$ is the unit vector in the radial direction. Thus for (5.1) we obtain that (5.5) reduces to

$$\rho(1) = \lambda. \tag{5.6}$$

The Euler–Lagrange equation for (5.3) is

$$\left(r\Phi_{,1}\left(\rho'(r), \frac{\rho(r)}{r}\right)\right)' = \Phi_{,2}\left(\rho'(r), \frac{\rho(r)}{r}\right), \qquad 0 < r < 1, \tag{5.7}$$

subject to (5.6) and

$$\rho(0) \geqslant 0, \ \lim_{r \to 0^+} r\Phi_{,1}\left(\rho'(r), \frac{\rho(r)}{r}\right) = 0. \tag{5.8}$$

The second condition in (5.8) states that if a hole opens at the center ($\rho(0) > 0$), then the component of the stress normal to the surface of the hole, is zero. For $\alpha < 2$ and $A = B$ in (4.8), Ball [1] proved that for λ sufficiently large, the minimizer of (5.3) satisfies (5.8) with $\rho(0) > 0$; i.e., a hole opens up at the center of the ball. This phenomena of void formation is called *cavitation*.

Let r_i be as x_i in (3.4). We discretize (5.3) as

$$I_h(\rho_h) = h\sum_{i=0}^{n-1} r_{i+1/2}\Phi^{i+1/2}, \tag{5.9}$$

where

$$\begin{aligned} & r_{i+1/2} = \frac{r_{i+1} + r_i}{2}, \\ & \Phi^{i+1/2} = \Phi\left(\frac{\rho_{i+1} - \rho_i}{h}, \frac{\rho_{i+1} + \rho_i}{r_{i+1} + r_i}\right), \qquad 0 \leqslant i \leqslant n-1, \end{aligned} \tag{5.10}$$

and $\rho_n = \lambda$. It follows now that for any v_h with $v_n = 0$ we have that

$$\delta I_h(\rho_h) \cdot v_h = h\sum_{i=1}^{n-1} [L_h(\rho_h)]_i v_i + hB_h(\rho_h) v_0, \tag{5.11}$$

where

$$\begin{aligned} [L_h(\rho_h)]_i = {} & -\frac{1}{h}(r_{i+1/2}\Phi_{,1}^{i+1/2} - r_{i-1/2}\Phi_{,1}^{i-1/2}) \\ & + \frac{1}{2}(\Phi_{,2}^{i+1/2} + \Phi_{,2}^{i-1/2}), \end{aligned} \tag{5.12}$$

$$B_h(\rho_h) = -\frac{1}{h} r_{1/2}\Phi_{,1}^{1/2} + \frac{1}{2}\Phi_{,2}^{1/2}, \qquad 1 \leqslant i \leqslant n-1.$$

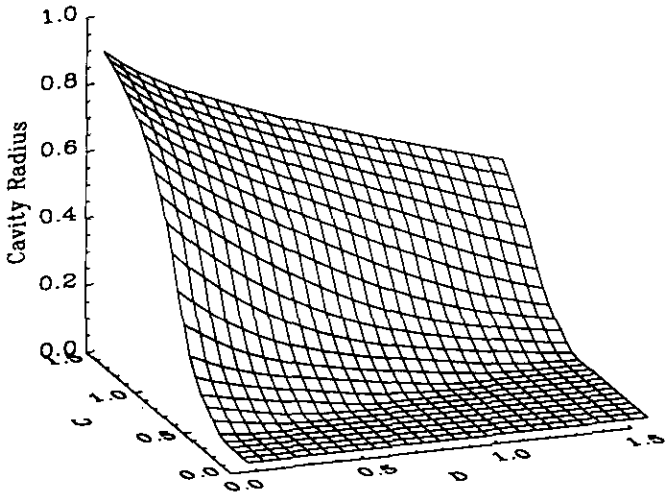

FIG. 5.1. Surface of the cavity radius as a function of C and D corresponding to $A = B = 1.0$, $\alpha = \gamma = \delta = 1.5$, and $\lambda = 1.2$.

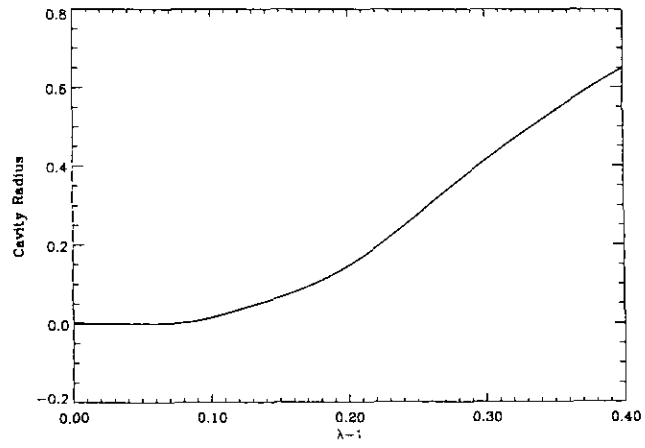

FIG. 5.3. Cavity radius as a function of the boundary displacement $\lambda - 1$ corresponding to $A = B = C = 1.0$ and $\alpha = 1.5$.

The second equation in (5.12) represents a free-boundary condition which is obtained from minimizing the functional (5.9) with respect to ρ_0 and its solution determines the cavity size. If the affine solution is stable, the solution to the free-boundary equation is $\rho_0 = 0$.

The following results where obtained using the accelerated steepest descent method of Section 2. We tested the code with $A = B = 1.0$, $\alpha = \gamma = \delta = 1.5$, $\lambda = 1.2$, and C, D arbitrary. In Fig. 5.1 we show the cavity radius of the equilibrium configuration computed by the code as a function of C and D. (Figure 5.2 shows several cross sections of this surface for different values of D.) We see from these figures that the cavity radius is very sensitive to changes in both C and D. We find that the cavity radius is increasing with C for D fixed. Since C is proportional to the energy due to changes in area, as C increases, the cavity radius increases to make the total area small. On the other hand, since the term proportional to D is inversely proportional to changes

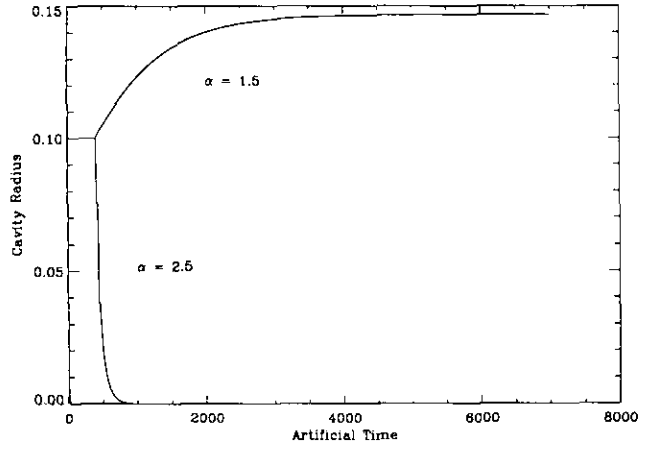

FIG. 5.4. The artificial time evolution of the cavity radius for $A = B = C = D = 1.0$, $\lambda = 1.2$, and different values of α.

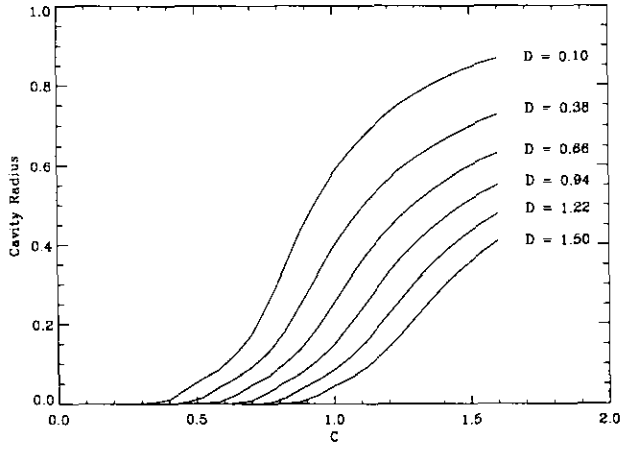

FIG. 5.2. Cross sections of the surface in Fig. 5.1.

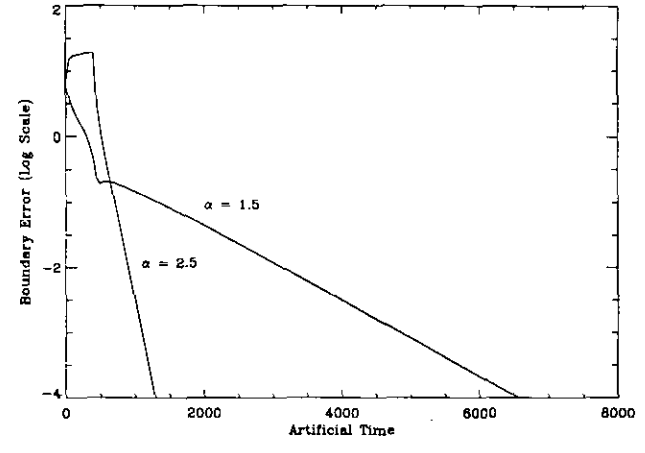

FIG. 5.5. The artificial time evolution of the boundary error corresponding to $A = B = C = D = 1.0$, $\lambda = 1.2$, and different values of α.

in the area, for C fixed and increasing D, the cavity radius should decrease (thus increasing the total area) as shown in the figures.

Note that the affine solution $\rho(s) = \lambda s$ is always a solution of (5.6)–(5.8). If $\alpha < 2$ and λ is sufficiently large, then the cavitated solution is stable and the scheme converges to this solution. If $\alpha > 2$, then the affine solution is stable for all λ and the scheme converges to this solution. Just for the case $\alpha = 1.5$, we show in Fig. 5.3 the cavity size of the equilibrium configuration computed by the code as a function of the boundary displacement $\lambda - 1$. Note that since the affine solution (cavity size zero) is always a solution (of both the continuous and discrete problems!), in Fig. 5.3 there is actually a bifurcation from the affine solution for $\lambda - 1$ in (0.08, 0.09) approximately. The fact that the code converges to the cavitated solution and not the affine for $\lambda - 1$ greater than 0.09 shows that the cavitated solution is stable in the energy sense for λ sufficiently large and, correspondingly, it shows that the affine solution is unstable, although it satisfies the Euler–Lagrange equations. These results are in agreement with those of Ball [1]. In Fig. 5.4 we show for $\alpha = 1.5$ and $\alpha = 2.5$ how the cavity size varies with the artificial time "k" in (2.10). In this figure $A = B = C = D = 1.0$, $\gamma = \delta = 1.5$, and $\lambda = 1.2$. On both cases the code starts iterating with an initial cavity size of 0.1 and does not "improve" on this until the first 400 iterations. For the same problems, Fig. 5.5 shows (in log scale) the inner boundary error (the second equation in (5.12)) as a function of the artificial time. From this we obtain that the rate of convergence of the inner boundary error is approximately exponential.

To estimate the basin of attraction of the cavitated solution when $\alpha = 1.5$, we show in Fig. 5.6 the time evolution of the cavity radius for different initial cavity sizes. Thus when the cavitated solution exists, it is stable and has a very large basin of attraction. Note that even starting with very small cavities close to the affine solution, the code still converges to the cavitated solution. On the other hand if $\alpha = 2.5$, so that the affine solution is stable according to the results in Ball [1], Fig. (5.7) shows that, essentially, starting with any cavity size, the code "closes up" the cavity and converges to the affine solution. Thus the situation here is very different from that of Section 3. The functional here has two critical points but only one is stable, depending on the sizes of α and λ.

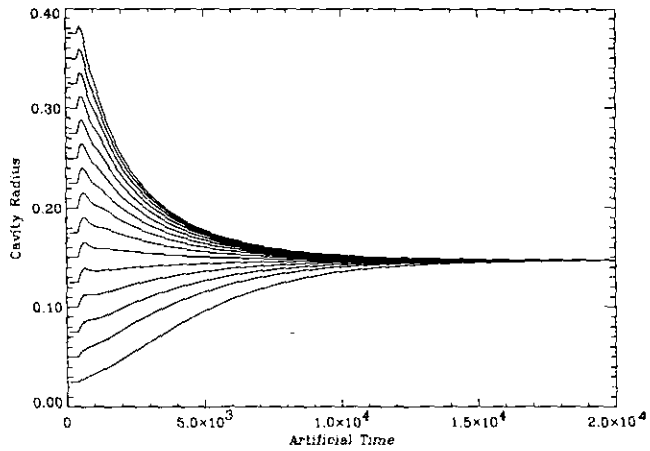

FIG. 5.6. The artificial time evolution of the cavity radius for $A = B = C = D = 1.0$, $\lambda = 1.2$, $\alpha = 1.5$, and different initial cavity sizes.

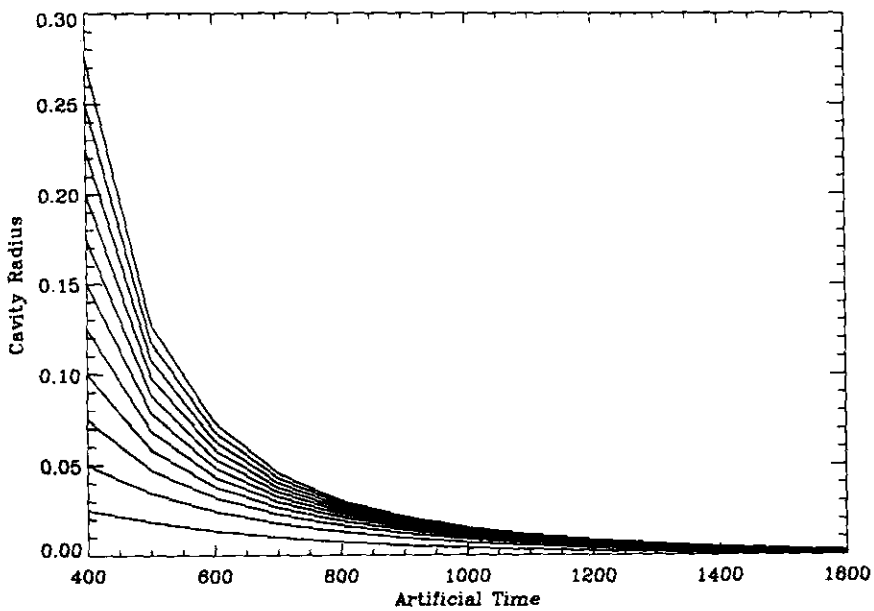

FIG. 5.7. The artificial time evolution of the cavity radius for $A = B = C = D = 1.0$, $\lambda = 1.2$, $\alpha = 2.5$, and different initial cavity sizes.

6. CAVITATION OF ARBITRARY DEFORMATIONS

Consider the problem of minimizing (4.5) subject to (4.7), (4.8), (4.9), (4.12), and (5.5). In this section we discuss how the method of Section 2 is used to solve numerically this problem.

Let (r, θ) be polar coordinates for Ω, let $(R(r, \theta), \Theta(r, \theta))$ be the polar coordinates of $p(x)$, and recall Eqs. (4.12). Define

$$\Lambda_{1,2} = R_r^2 + \frac{1}{r^2} R_\theta^2 \pm \left(\Theta_r^2 + \frac{1}{r^2} \Theta_\theta^2 \right) R^2, \tag{6.1a}$$

$$\Lambda_3 = 2 \left(R_r \Theta_r + \frac{1}{r^2} R_\theta \Theta_\theta \right) R, \tag{6.1b}$$

$$\Lambda_4 = [\Lambda_2^2 + \Lambda_3^2]^{1/2}, \tag{6.1c}$$

$$L_2 = \frac{\Lambda_2}{\Lambda_4}, \qquad L_3 = \frac{\Lambda_3}{\Lambda_4}. \tag{6.1d}$$

Thus from (4.12) we find that

$$v_{1,2}^2 = \tfrac{1}{2} [\Lambda_1 \pm \Lambda_4]. \tag{6.2}$$

Let

$$w_1 = v_1^2, \qquad w_2 = v_2^2, \tag{6.3a), (6.3b)}$$

$$\phi(w_1, w_2) = \Phi(w_1^{1/2}, w_2^{1/2}). \tag{6.4}$$

The Euler–Lagrange equations for (4.5), (4.7) are thus given by

$$\begin{aligned} &-\frac{\partial}{\partial r} \{ r(\phi_{,1} + \phi_{,2} + (\phi_{,1} - \phi_{,2}) L_2) R_r \} \\ &\quad - R \frac{\partial}{\partial r} \{ r(\phi_{,1} - \phi_{,2}) L_3 \Theta_r \} \\ &\quad - \frac{\partial}{\partial \theta} \left\{ \frac{1}{r} (\phi_{,1} + \phi_{,2} + (\phi_{,1} - \phi_{,2}) L_2) R_\theta \right\} \\ &\quad - R \frac{\partial}{\partial \theta} \left\{ \frac{1}{r} (\phi_{,1} - \phi_{,2}) L_3 \Theta_\theta \right\} \\ &\quad + r(\phi_{,1} + \phi_{,2} - (\phi_{,1} - \phi_{,2}) L_2) R \left(\Theta_r^2 + \frac{1}{r^2} \Theta_\theta^2 \right) = 0, \end{aligned} \tag{6.5a}$$

$$\begin{aligned} &-\frac{\partial}{\partial r} \{ r(\phi_{,1} + \phi_{,2} - (\phi_{,1} - \phi_{,2}) L_2) \Theta_r R^2 \\ &\quad + r(\phi_{,1} - \phi_{,2}) L_3 R R_r \} \\ &\quad - \frac{\partial}{\partial \theta} \left\{ \frac{1}{r} (\phi_{,1} + \phi_{,2} - (\phi_{,1} - \phi_{,2}) L_2) \Theta_\theta R^2 \right. \\ &\quad \left. + \frac{1}{r} (\phi_{,1} - \phi_{,2}) L_3 R R_\theta \right\} = 0, \end{aligned} \tag{6.5b}$$

where the arguments of $\phi_{,1}$, $\phi_{,2}$ are (w_1, w_2).

The boundary condition (5.5) takes the form

$$R(1, \theta) = \lambda, \qquad \Theta(1, \theta) = \theta, \qquad \theta \in [0, 2\pi). \tag{6.6}$$

The natural boundary conditions for (6.5) are given by

$$\begin{aligned} \lim_{r \to 0^+} &r\{(\phi_{,1} + \phi_{,2} + (\phi_{,1} - \phi_{,2}) L_2) R_r \\ &+ (\phi_{,1} - \phi_{,2}) L_3 R \Theta_r \} = 0, \end{aligned} \tag{6.7a}$$

$$\begin{aligned} \lim_{r \to 0^+} &r\{(\phi_{,1} + \phi_{,2} - (\phi_{,1} - \phi_{,2}) L_2) R^2 \Theta_r \\ &+ (\phi_{,1} - \phi_{,2}) L_3 R R_r \} = 0. \end{aligned} \tag{6.7b}$$

These equations represent the free-boundary condition that determines the shape of the cavity. We also have that the periodicity conditions

$$R, \Theta - \theta, \Theta_\theta, \Theta_r, R_\theta, R_r, \text{ are periodic in } \theta. \tag{6.8}$$

For any integers $n, m \geq 1$, let

$$\begin{aligned} &h = \frac{1}{n}, \qquad r_i = ih, \qquad 0 \leq i \leq n, \\ &k = \frac{2\pi}{m}, \qquad \theta_j = jk, \qquad 0 \leq j \leq m. \end{aligned} \tag{6.9}$$

For any function u of (r, θ), we let u_{ij} denote an approximation of $u(r_i, \theta_j)$. We now approximate $u_r(r_{i+1/2}, \theta_j)$ by

$$u_r(r_{i+1/2}, \theta_j) \approx \delta u_{ij} \doteq \frac{u_{i+1,j} - u_{ij}}{h}, \tag{6.10}$$

$0 \leq i < n$, $0 \leq j < m$. For the derivatives in the "θ" direction we use a truncated Fourier series. More specifically, let $\{u_{ij}\}$, $0 \leq i \leq n$, $0 \leq j \leq m$, be a mesh function defined over (6.9) and let

$$u_{ij} = \sum_{|\alpha| \leq N} a_\alpha(r_i) \, e^{i\alpha\theta_j}, \tag{6.11}$$

$0 \leq i < n$, $0 \leq j < m$, be its discrete Fourier representation. We now compute

$$u_{\theta,ij} = \sum_{|\alpha| \leq N} i\alpha a_\alpha(r_i) \, e^{i\alpha\theta_j}, \tag{6.12}$$

$0 \leq i < n$, $0 \leq j < m$. Numerically, to compute (6.12), we first compute the $\{a_\alpha\}$ in (6.11) using an FFT routine; then we compute the $\{i\alpha a_\alpha\}$, and finally we use an inverse FFT routine to obtain the mesh representation of u_θ. Expansions like $u_{\theta,i+1/2,j}$ now have the meaning

$$u_{\theta,i+1/2,j} = \tfrac{1}{2}(u_{\theta,i+1,j} + u_{\theta,ij}), \tag{6.13}$$

$0 \leqslant i < n$, $0 \leqslant j < m$, where $u_{\theta,i+1,j}$ and $u_{\theta,ij}$ come from (6.12). With the formulas (6.10), (6.12), and (6.13) we discretize (6.1) as

$$\Lambda_{1,2,i+1/2,j} = (\delta R_{ij})^2 + \frac{1}{r_{i+1/2}^2}\left\{\frac{R_{\theta,i+1,j}^2 + R_{\theta,ij}^2}{2}\right\} \pm \left((\delta\Theta_{ij})^2 + \frac{1}{r_{i+1/2}^2}\left\{\frac{\Theta_{\theta,i+1,j}^2 + \Theta_{\theta,ij}^2}{2}\right\}\right) \times R_{i+1/2,j}^2, \tag{6.14}$$

$0 \leqslant i < n$, $0 \leqslant j < m$, etc., and

$$w_{1,2,i+1/2,j} = \tfrac{1}{2}[\Lambda_{1,i+1/2,j} \pm \Lambda_{4,i+1/2,j}], \tag{6.15}$$

$0 \leqslant i < n$, $0 \leqslant j < m$. Now we discretize (4.5), (4.7) by

$$I_h(R_h, \Theta_h) = hk \sum_{i=0}^{n-1} \sum_{j=0}^{m-1} r_{i+1/2} \Phi^{i+1/2,j}, \tag{6.16a}$$

where

$$\Phi^{i+1/2,j} = \Phi(w_{1,i+1/2,j}, w_{2,i+1/2,j}), \tag{6.16b}$$

$0 \leqslant i < n$, $0 \leqslant j < m$, and $R_h = \{R_{ij}\}$, $\Theta_h = \{\Theta_{ij}\}$. The combination of (6.10), (6.12), (6.13) with the method of Section 2, applied to (6.16), is called a *spectral-collocation method* (see [6]).

We tested the code with $A = B = C = D = 1.0$, $\alpha = \gamma = \delta = 1.5$, $\lambda = 1.2$, and $n = 20$, $m = 32$. The various initial configurations used in (2.10), where (here u_0, β, and the d's are nonnegative numbers and the n's are positive integers) for the $\{R_{ij}\}$ we use either

$$R_{ij} = u_0(1 + d_1 \cos n_1\theta_j + d_2 \sin n_2\theta_j) \times (1 - r_i^\beta) + \lambda r_i^\beta, \quad 0 \leqslant i \leqslant n, \quad 0 \leqslant j \leqslant m. \tag{6.17a}$$

or

$$R_{ij} = u_0 + (\lambda - u_0)(1 + d_3 \cos n_3\theta_j + d_4 \sin n_4\theta_j)\, r_i^\beta + (d_5 \cos n_5\theta_j + d_6 \sin n_6\theta_j)\, r_i(1 - r_i), \quad 0 \leqslant i \leqslant n, \quad 0 \leqslant j \leqslant m. \tag{6.17b}$$

For the $\{\Theta_{ij}\}$ we use either

$$\Theta_{ij} = \theta_j + c_1 r_i(1 - r_i), \qquad 0 \leqslant i \leqslant n, \quad 0 \leqslant j \leqslant m, \tag{6.18a}$$

or

$$\Theta_{ij} = \theta_j + c_2 \sin 2\pi r_i, \qquad 0 \leqslant i \leqslant n, \quad 0 \leqslant j \leqslant m, \tag{6.18b}$$

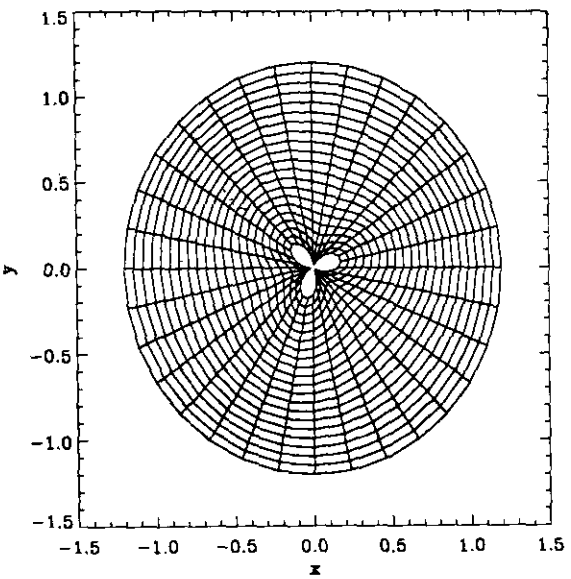

FIG. 6.1. Initial configuration corresponding to Case 1.

where the c's are nonnegative numbers. For (6.17a) the inner cavity at $r = 0$ need not be circular but the outer edge at $r = 1$ is always circular with radius λ. For (6.17b), on the contrary, the inner radius is always circular with radius u_0 while the outer edge need not be circular. We considered the following particular cases of these initial conditions. In all cases $u_0 = 0.1$ and $\beta = 1.0$.

Case 1. Initial conditions (6.17a) and (6.18a) with $d_1 = d_2 = 0.6$, $n_1 = n_2 = 3$, and $c_1 = 0.0$. The graph is shown in Fig. 6.1.

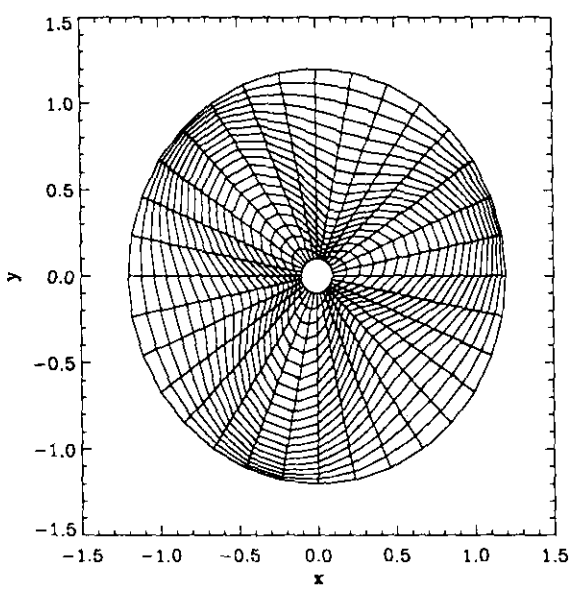

FIG. 6.2. Initial configuration corresponding to Case 2.

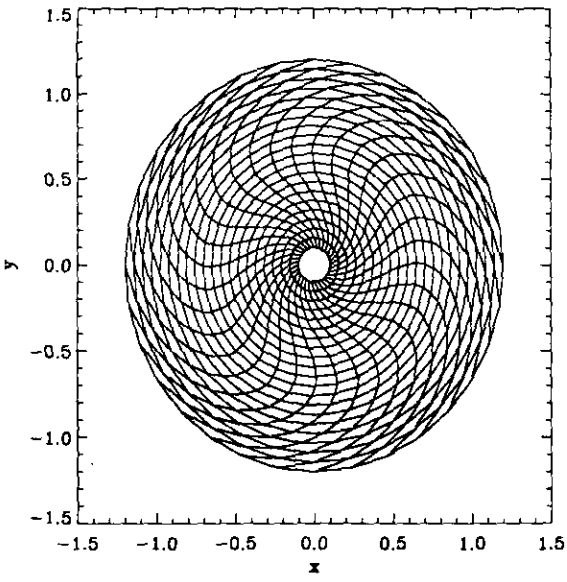

FIG. 6.3. Initial configuration corresponding to Case 3.

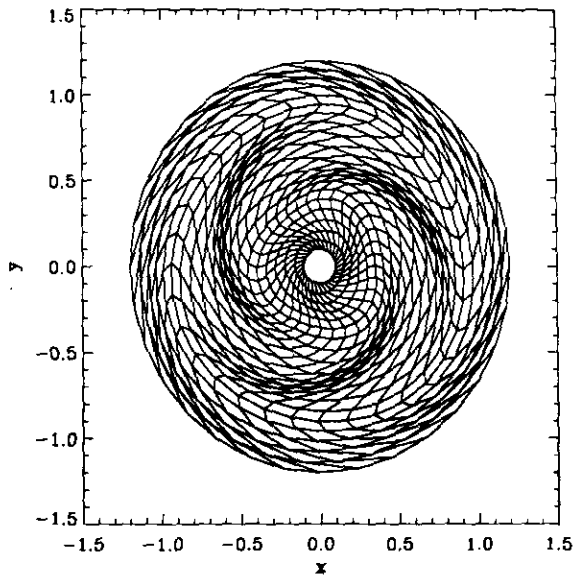

FIG. 6.5. Initial configuration corresponding to Case 5.

Case 2. Initial conditions (6.17b) and (6.18a) with $d_3 = d_4 = 0.0$, $d_5 = d_6 = 0.6$, $n_5 = n_6 = 3$, and $c_1 = 0.0$. The graph is shown in Fig. 6.2.

Case 3. Initial conditions (6.17b) and (6.18a) with $d_3 = d_4 = d_5 = d_6 = 0.0$ and $c_1 = 4.0$. The graph is shown in Fig. 6.3.

Case 4. Initial conditions (6.17b) and (6.18a) with $d_3 = d_4 = 0.0$, $d_5 = d_6 = 0.1$, $n_5 = n_6 = 3$, and $c_1 = 4.0$. The graph is shown in Fig. 6.4.

Case 5. Initial conditions (6.17b) and (6.18b) with $d_3 = d_4 = 0.0$, $d_5 = d_6 = 0.1$, $n_5 = \times n_6 = 3$, and $c_2 = 1.0$. The graph is shown in Fig. 6.5.

We also show in Fig. 6.6 an initial configuration not described by (6.17), (6.18), with an ellipsoidal cavity. Each of these initial configurations satisfy (5.5) or, equivalently, (6.6). (In the figures of configurations, the radial lines correspond to "θ" constant and the circumferential lines correspond to "r" constant). In all of these cases the code converges to the radially symmetric solution of Section 5 corresponding to the same data. The inner cavity radius is approximately 0.147. The graph of the final configuration is shown in Fig. 6.7. In Fig. 6.8 we show the determinant of the deformation gradient (4.2) as a function of (r, θ). This figure shows that in the final configuration the deformation across the body is nearly constant except close to the inner cavity

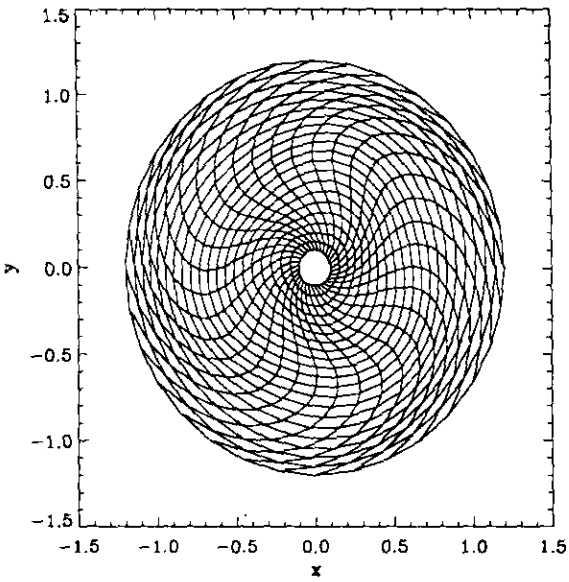

FIG. 6.4. Initial configuration corresponding to Case 4.

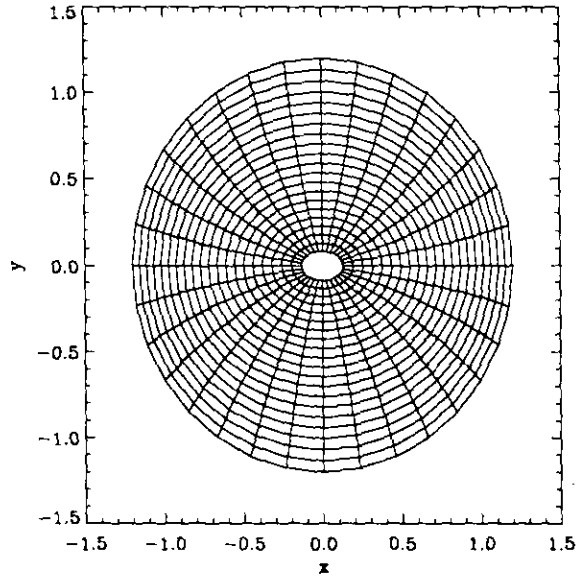

FIG. 6.6. Initial configuration with ellipsoidal cavity.

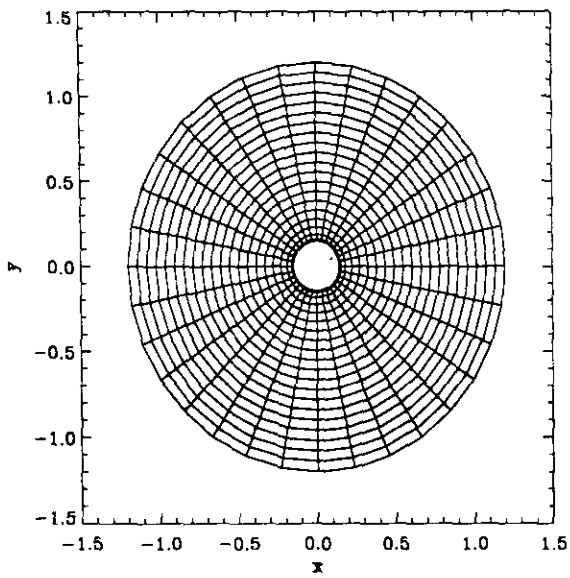

FIG. 6.7. *Final configuration (axisymmetric) computed by the code* corresponding to the initial configurations in Figs. 6.1.–6.6.

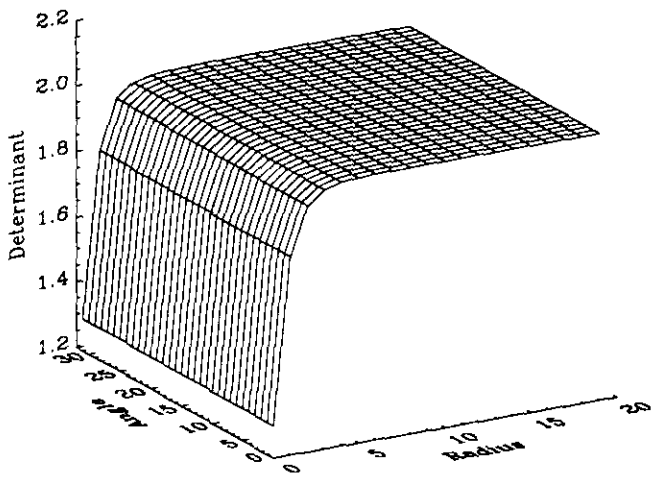

FIG. 6.8. Determinant of the deformation gradient for the final deformation in Fig. 6.7.

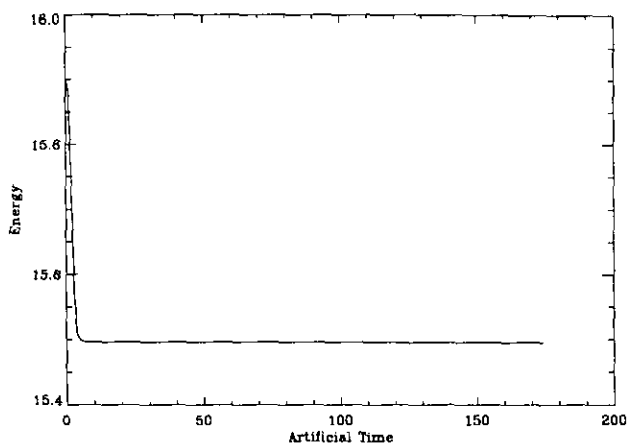

FIG. 6.9. The artificial time evolution for the energy corresponding to *Case 1.*

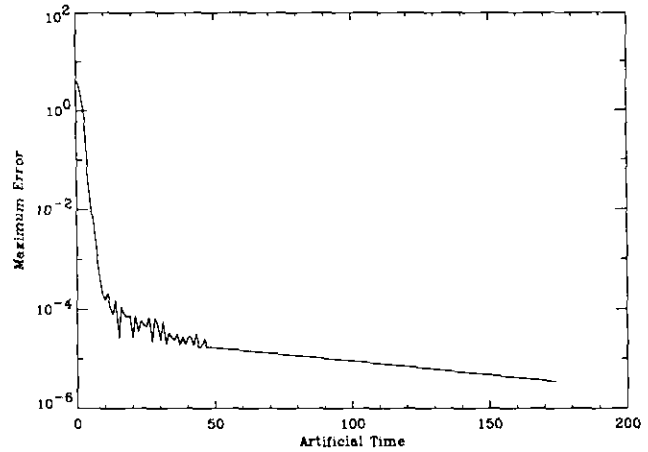

FIG. 6.10. The artificial time evolution of the maximum interior error *for Case 1.*

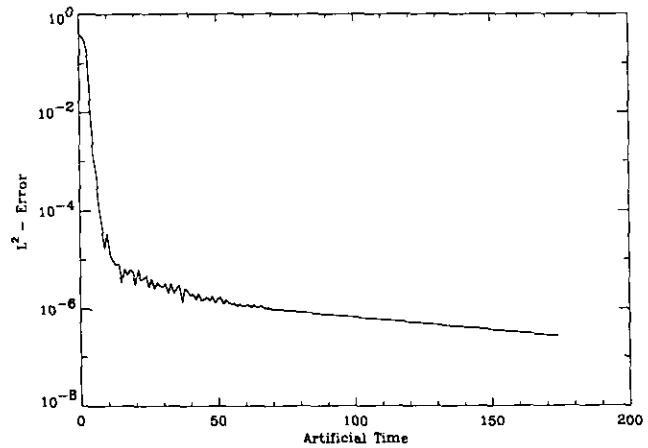

FIG. 6.11. The artificial time evolution of the interior L^2 error for Case 1.

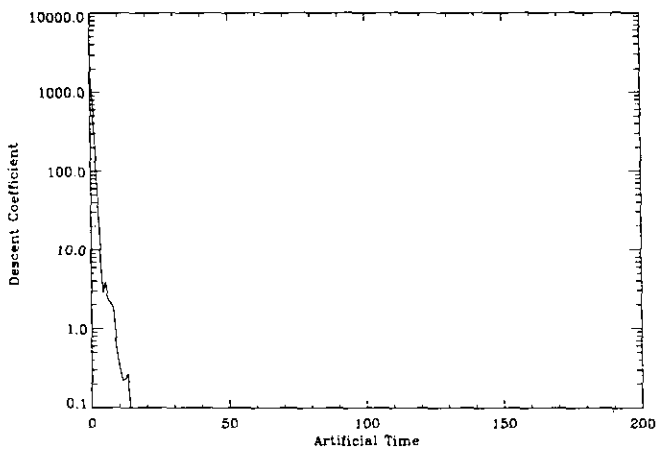

FIG. 6.12. The artificial time evolution of the descent coefficient for *Case 1.*

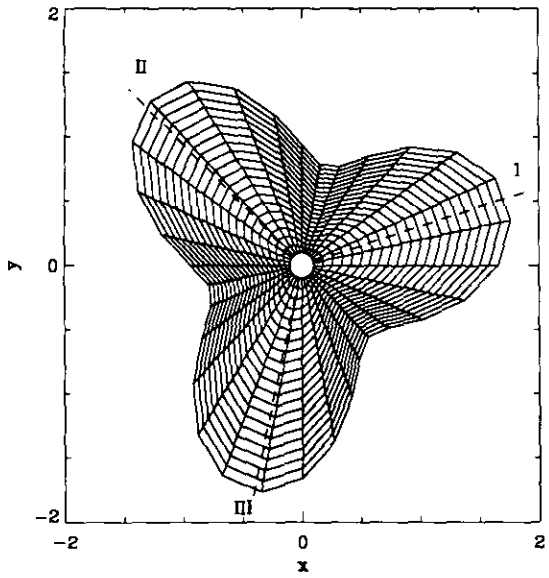

FIG. 6.13. Initial configuration corresponding to Case 6.

where the material is highly compressed (compared to rest of the body).

Just for Case 1 (the other cases are similar), we show in Figs. 6.9–6.12, as a function of the artificial time "k" in (2.10), the graphs of the energy, the maximum norm, and discrete L_2 norm of the Fourier coefficients of the first variation of (6.16a), and the descent coefficient (the "ε" in (2.10)) estimated by the code. (See [4, 5, 6] for a discussion of how ε is estimated.) From Figs. 6.10, 6.11 we obtain an approximate exponential convergence on the error as measured by the size of the first variation. (The convergence is actually exponential when (2.10) is applied to (2.3) or, in general, for any linear elliptic operator.)

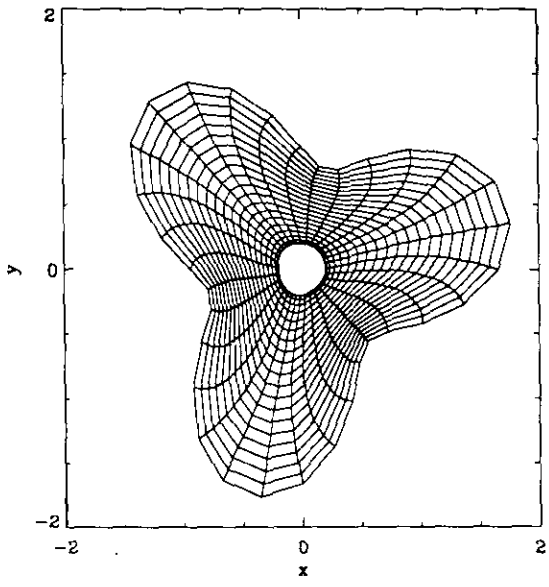

FIG. 6.14. Final configuration corresponding to Case 6.

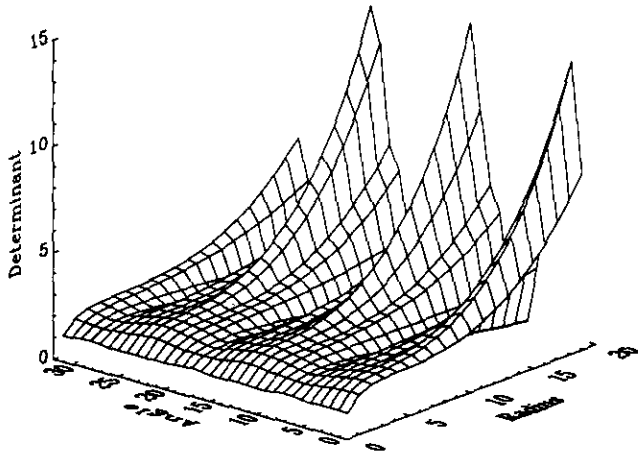

FIG. 6.15. Determinant of the deformation gradient for the final configuration in Fig. (6.14).

We also considered the following case in which the outer boundary of the initial configuration is noncircular:

Case 6: Initial conditions (6.17b) and (6.18a) with $d_3 = d_4 = 0.3$, $d_5 = d_6 = 0.0$, $n_3 = n_4 = 3$, $u_0 = 0.1$, $\lambda = 1.3$, and $c_1 = 0.0$. The graph is shown in Fig. 6.13.

The final configuration is shown in Fig. 6.14. Note the changes on the radial and circumferential lines as well as the inner cavity which is noncircular. The discrete energies of the initial and final configurations are 22.48 and 20.49, respectively. In Fig. (6.15) we show the determinant of the deformation gradient (4.2) for this problem. Note again that the inner cavity is in a state of high compression. The regions of high deformation (large determinant) correspond to the sectors labelled I, II, and III in Fig. 6.13.

7. CONCLUSIONS AND COMMENTS

When the physical parameters in (4.8) are such that the cavitated solution is stable, then the axisymmetric cavitated solution appears to be the global minimum and has a very large basin of attraction. We tried a host of initial configurations shown in Figs. 6.1–6.6 and with cavities of other shapes, and always the code converges to the axisymmetric cavitated solution. Also Fig. 5.6 gives an estimate of the domain of attraction of the axisymmetric cavitated minima as a function of the initial cavity size. If the parameters in (4.8) are such that the affine solution (no cavitation) is stable, then the code finds this solution as the global minimum even for initial conditions with a cavity (see Fig. 5.7).

The initial conditions in Figs. 6.1–6.6 all correspond to a uniform displacement of the boundary (the displacements in the interior are nonuniform). The fact that the code converges in all cases to the axisymmetric solution of Section 5, is a strong indication of the global stability of this solution.

TABLE I

n	$e(\rho_n)$	$e(\rho_n)/e(\rho_{2n})$
4	0.329365E + 00	—
8	0.236298E + 00	0.717432E + 00
16	0.146077E + 00	0.618189E + 00
32	0.730892E − 01	0.500349E + 00
64	0.259182E − 01	0.344611E + 00

(This does not contradict the results of James and Spector [12] as their results are three dimensional). Moreover, the code is able to compute a fully two-dimensional solution (Fig. 6.14) when the boundary displacement is nonuniform.

For the one-dimensional problem of Section 5 with $\rho_0 = 0$, our method has a rate of convergence of $O(h^2)$ if the function ρ is smooth and, in general, is $O(h)$ if the solution has an unbounded derivative. (See [11].) For the case $\rho_0 > 0$ and the data $A = B = C = D = 1.0$, $\gamma = \delta = 1.5$, and $\lambda = 1.2$, we computed solutions corresponding to $n = 4, 8, ..., 64$ and used the solution corresponding to $n = 128$ as the exact discretized solution for the purpose of estimating the errors. We use the notation

$$e(\rho_n) = \|\rho_n - \rho_{128}\|_\infty,$$

where ρ_n stands for the solution ρ_h, corresponding to $h = 1/n$. (Here we understand that in $\rho_n - \rho_{128}$ only the components of ρ_{128} corresponding to those of ρ_n are used in the computation.) The results are shown in Table I which shows an approximate rate of convergence of $O(h^{3/2})$ in this case. The full analysis of the method of Section 6 shall be pursued elsewhere.

The combination of the Richardson extrapolation technique and the spectral-collocation method has proven to be a powerful and robust method in this problem as well as in applications to plasma physics for instance (see [6]). One can obtain further speedup in the performance of the method if some kind of pre-conditioning is used in (2.10). We are currently working on a follow up paper in which we discuss a pre-conditioning that has been used in the three-dimensional MHD problem of plasma physics, which results in a scheme requiring $O(1)$ iterations, and that has the advantage of preserving descent and requires a minimal overhead (less than 1%) for the pre-conditioned steps. The use of multigrids, although attractive, might lead to a scheme which does not have the descent property.

ACKNOWLEDGMENTS

This work was supported in part by the National Science Foundation under Grant Number DMS-8722521 and EPSCoR of Puerto Rico (Negrón-Marrero), and by the CUNY-UPR Academic Exchange Program (Betancourt).

REFERENCES

1. J. M. Ball, *Phil. Trans. R. Soc. London A* **306**, 557 (1982).
2. J. M. Ball, and G. Knowles, *Numer. Math.* **51**, 181 (1987).
3. J. M. Ball and V. J. Mizel, *Bull. Am. Math. Soc., New Ser.* **11**, 143 (1984).
4. F. Bauer, O. Betancourt, and P. R. Garabedian, *A Computational Method in Plasma Physics* (Springer-Verlag, New York, 1978).
5. F. Bauer, O. Betancourt, and P. R. Garabedian, *Magnetic Hydrodynamic Equilibrium and Stability of Stellarators* (Springer-Verlag, New York, 1984).
6. O. Betancourt, *Commun. Pure Appl. Math.* **4**, 551 (1988).
7. P. R. Garabedian, *Partial Differential Equations* (Wiley, New York, 1964).
8. A. N. Gent and P. B. Lindley, *Proc. R. Soc. London A* **249**, 195 (1958).
9. M. Lavrentiev, *Ann. Math. Pure Appl.* **4**, 7 (1926).
10. P. V. Negrón-Marrero, *Numer. Math.* **58**, 135 (1990).
11. P. V. Negrón-Marrero and C. Carbonera, *Numer. Math.* **56**, 93 (1989).
12. R. D. James and S. J. Spector, *The Formation of Filamentary Voids in Solids*, IMA Preprint Series, Vol. 572, (Inst. Math. Appl., Southend-on-Sea, 1989).
13. J. Sivaloganathan, *Arch. Rational Mech. Anal.* **96**, 589 (1988).
14. C. A. Stuart, *Ann. Inst. H. Poincare: Nonlinear Anal.* **2**, 33 (1985).